J Seismol
https://doi.org/10.1007/s10950-025-10330-y

RESEARCH

Seismicity and active seismic structures in the Valle de la Trinidad, Baja California, Mexico

Boris Rösler · Oscar Castro-Artola · Alejandra Martínez · Carlos E. Reinoza · Luis A. Yegres H. · J. Antonio Vidal-Villegas · Franck A. Audemard M.

Received: 15 May 2025 / Accepted: 27 August 2025

Abstract The Valle de la Trinidad region in northern Baja California is situated within a seismically active zone at the boundary between the Pacific and North American plates, characterized by complex fault interactions and significant crustal deformation. We investigate the seismicity of this region between 2010 and 2024 to better characterize active structures and earthquake interactions. Using waveform-based double-difference relocation, we refine the hypocentral locations of 4010 earthquakes with magnitudes ranging from ML 0.3 to 5.1 recorded by the Seismic Network of Northwest Mexico (RESNOM), significantly reducing epicentral and depth uncertainties. The relocated seismicity reveals clear alignment with the San Miguel fault and a previously unmapped intersecting structure, indicating that both faults are actively accommodating regional strain. Moment tensor inversions of the events with ML ≥ 4 show consistent right-lateral strike-slip mechanisms, with nodal planes aligned with both structures, although ambiguity remains regarding the exact fault that ruptured. The August 17, 2020 seismic sequence, initiated by an ML 4.7 foreshock and an ML 5.1 mainshock, demonstrates that triggering across intersecting faults may control rupture evolution. Temporal changes in focal mechanisms, from strike-slip to normal faulting, suggest stress field variations during the sequence. These results highlight the seismotectonic complexity of fault intersections in the Peninsular Ranges and emphasize the need to reassess seismic hazard models to incorporate the role of previously unmapped structures.

Keywords Baja California peninsula · Valle de la Trinidad · Seismicity · Relocation of epicenters · Moment tensor inversion · Seismic sequence

B. Rösler (✉) · O. Castro-Artola · A. Martínez · C. E. Reinoza · L. A. Yegres H. · J. A. Vidal-Villegas · F. A. Audemard M.
Center for Scientific Research and Higher Education at Ensenada (CICESE), Department of Seismology, Carretera Ensenada - Tijuana No. 3918, Zona Playitas, CP. 22860, Ensenada, B.C., Mexico
e-mail: boris@cicese.mx

F. A. Audemard M.
Universidad Central de Venezuela, Caracas, Venezuela

1 Introduction

The Baja California Peninsula lies along the tectonic boundary between the Pacific and North American plates and hosts a complex network of active faults that accommodate the relative plate motion. Faults are predominantly oriented northwest-southeast and exhibit a range of faulting types, including strike-slip, dip-slip, and oblique-slip displacements (Angelier et al. 1981). This structural fabric reflects the long-term evolution of the plate boundary from a convergent to a transform regime following the cessation of subduction along the western margin of North America during the late Miocene (Atwater 1970).

To the north, the Southern California Shear Zone (SCSZ) accommodates approximately 20-25% of the total Pacific-North America plate boundary motion (Dixon et al. 2000; Dokka and Travis 1990a, b; Miller

Published online: 09 September 2025

et al. 2001; Sauber et al. 1986, 1994; Savage et al. 1990; Thatcher et al. 2016). This broad, diffuse zone of dextral shear, approximately 125 km wide, encompassing a complex system of faults that extend across oceanic crust, coastal ranges, and inland domains. These faults exhibit a wide range of displacement rates and slip behaviors, including both locked and creeping segments, and contribute significantly to regional seismic hazard (Sauber et al. 1986; Savage et al. 1990).

Southward, the SCSZ transitions into the Baja California microplate (Dixon et al. 2000; Plattner et al. 2007), a tectonic block moving semi-independently between the Pacific and North American plates. The northern boundary of the microplate is delineated by several active fault systems, among which the San Miguel-Vallecitos fault system is particularly active (Bennett et al. 1996; Johnson et al. 1976; Shor and Roberts 1958). The San Miguel and Vallecitos faults — the northwestern and southeastern segments of this fault system —, accommodate right-lateral strike-slip motion, extending southeastward for approximately 160 km from the U.S.-Mexico border to their intersection with the Agua Blanca, Sierra de Juárez, and San Pedro Mártir faults. These intersections represent zones of structural complexity and are critical for understanding the dynamics of strain transfer across the boundary.

The San Miguel Fault exhibits an estimated slip rate of 3 ± 3 mm/yr (Bennett et al. 1996) and has been associated with at least six strong earthquakes ($M \geq 6$) between 1954 and 1956, with rupture lengths of approximately 20 km (Hirabayashi et al. 1996). In contrast, the Vallecitos Fault has not been clearly associated with recent large-magnitude seismic events, although the Mw 5.7 Guadalupe earthquake of 1949 may have occurred on this structure (Reyes et al. 1975). Due to its spatial proximity and similar structural orientation, the Tres Hermanos Fault is considered part of this broader fault system. Toward the south, the Agua Blanca and San Pedro Mártir faults define the southern margin of the system and the edge of the Baja California microplate. These faults exhibit slightly higher slip rates compared to faults to the north and play an important role in accommodating microplate motion (Bennett et al. 1996).

On August 17, 2020, a ML 5.1 earthquake occurred near the junction of these major fault systems in the Valle de la Trinidad, initiating a seismic sequence that persists to the present. The distribution of epicenters delineates linear trends that align with the mapped trace of the San Miguel Fault and a cross-cutting geological structure, suggesting active deformation along both the primary fault and a secondary, intersecting zone of structural weakness (Fig. 1). Notably, the location of the 2020 mainshock closely corresponds with the epicentral area of a Mw 6.3 earthquake that occurred in 1956, which was part of a sequence of three $M \geq 6$ events linked to a cross fault between the San Miguel and Sierra Juarez fault zones (Doser 1992). This interpretation is supported by relocations conducted using the bootstrap relocation routine of Petroy and Wiens (1989), which Doser (1992) used in her analysis. The similarity in source mechanisms, magnitudes, and locations suggests that the 2020 sequence may represent reactivation of the San Miguel Fault system, with triggered rupture along a cross-cutting structure.

In addition to the 1956 sequence, the Valle de la Trinidad region has experienced several other moderate events, including earthquakes in 1975 (M 5.1), 1985 (M 5.4), 1988 (M 5.3), 1991 (M 5.4), and 1994 (M 5.3), as well as lower-magnitude events in 1994 and 1996 (M 4.1-4.3; Vidal et al. 2010). The clustering of these events underscores the persistent seismogenic activity in this structurally complex zone and reinforces its potential for future damaging earthquakes.

It is noteworthy that not all large earthquakes in the Valle de la Trinidad region have been associated with sustained aftershock activity. For example, the ML 5.1 earthquake in 2015 produced only a brief aftershock sequence, followed by nearly two years of relative seismic quiescence before seismicity resumed at elevated rates. This variability in post-seismic behavior highlights the complexity of fault interaction and stress redistribution processes in the region.

During the ongoing seismic sequence initiated in 2020, a total of 2862 earthquakes were recorded up to the end of 2024, with magnitudes ranging from ML 0.3 to 5.1. In this study, we analyze the seismicity of the past 15 years in northern Baja California by precisely relocating earthquake hypocenters and correlating them with mapped geologic faults. This approach enables the identification of active, potentially seismogenic structures and offers critical insight into fault interaction processes, rupture dynamics, and the region's seismic hazard, including the potential for future large earthquakes.

The seismicity observed to the south and southeast of the study area suggests the possible existence of blind or previously unrecognized fault structures. In

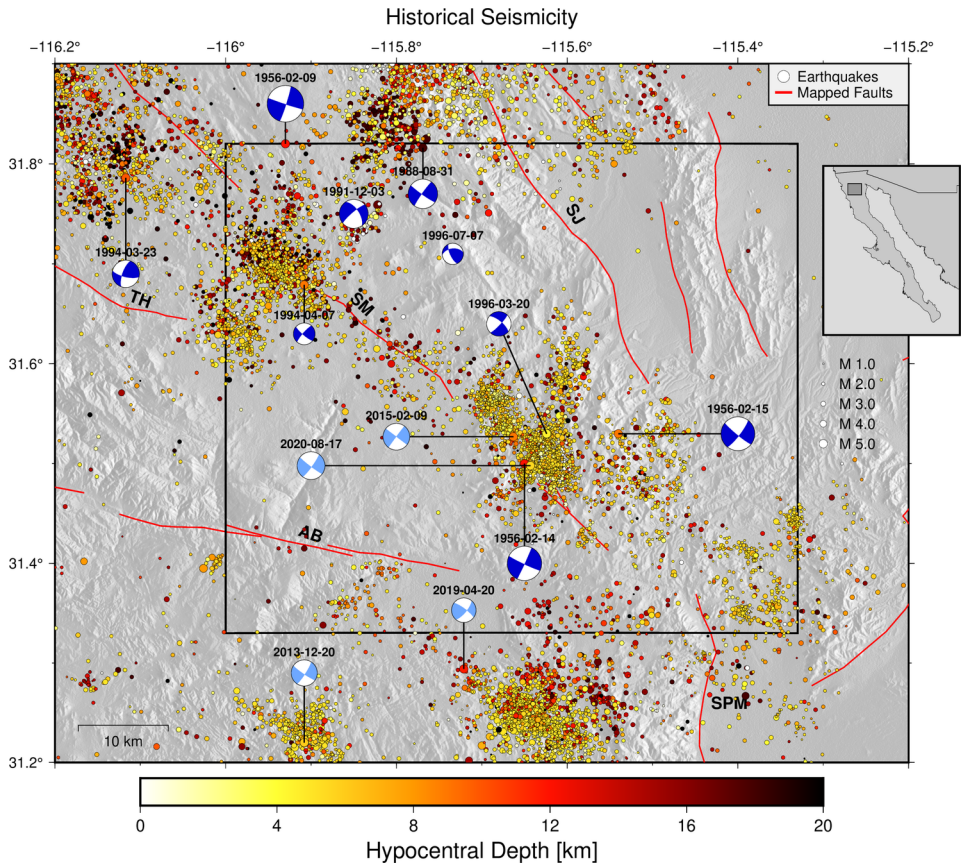

Fig. 1 Geologic setting of the Valle de la Trinidad at the junction of the Agua Blanca (AB), Tres Hermanos (TH), San Miguel (SM), San Pedro Mártir (SPM), and Sierra Juárez (SJ) faults. The map shows the focal mechanisms of nine historical earthquakes from 1956 until 1996 with magnitudes M ≥ 4 (Vidal et al. 2010), as well as the hypocenters of digitally recorded events since 1976 in the RESNOM catalog. Focal mechanisms for earthquakes in 2013, 2015, 2019, and 2020 — as determined by the United States Geological Survey (USGS) — are displayed

particular, the spatial distribution of epicenters indicates a coherent seismic cluster in this region, similar to what is observed in the Valle de la Trinidad. Notably, the hypocentral depths within this cluster appear to increase from southwest to northeast, hinting at underlying geological features such as dipping fault planes that remain poorly characterized. These observations highlight the need for further structural investigations in this part of the region.

2 Data

Seismicity in the Valle de la Trinidad forms a distinct cluster that is geographically separated from earthquake epicenters associated with other fault systems in the region. As such, this study focuses on a rectangular area bounded between 31.33 and 31.82° latitude and -115.33 and −116.00° longitude, centered at the intersection of the Sierra Juárez (SJ), San Miguel (SM), Agua Blanca (AB), and San Pedro Mártir (SPM) faults (Fig. 1). Earthquake data were obtained from the catalogs of the Seismic Network of Northwest Mexico (RESNOM) and the Northwest Mexico Accelerograph Network (RANM, Vidal-Villegas et al. 2018), both operated by the Center for Scientific Research and Higher Education at Ensenada (CICESE). These networks were designed to detect, record, and catalog seismic activity throughout northwestern Mexico, particularly in northern Baja California and northwestern Sonora. The RESNOM network currently comprises 29 seismic stations, while RANM has 19. Following the

2010 El Mayor-Cucapah earthquake, coverage in the study area was significantly improved by the installation of additional stations, enhancing the sensitivity and spatial resolution of the networks.

In addition to RESNOM and RANM, seismic stations from the Broadband Seismological Network of the Gulf of California (RESBAN, Castro et al. 2018), the Southern California Seismic Network (SCSN, Hutton et al. 2006), and the Mexican National Seismological Service (SSN, Pérez-Campos et al. 2018) were used to supplement earthquake locations in the study (Fig. 2).

Seismic waveforms are initially analyzed using a short-term average/long-term average (STA/LTA) algorithm, which automatically detects events by comparing the signal's average amplitude over a short window (STA) to that over a longer window (LTA). When the STA/LTA ratio exceeds a threshold, a potential seismic event is flagged for further analysis. An initial hypocentral location is estimated by triangulating the earthquake's position based on the P- and S-wave arrival time differences at each station. This estimate is then refined by an analyst who manually reviews and adjusts the P- and S-wave picks. Local magnitude (ML)

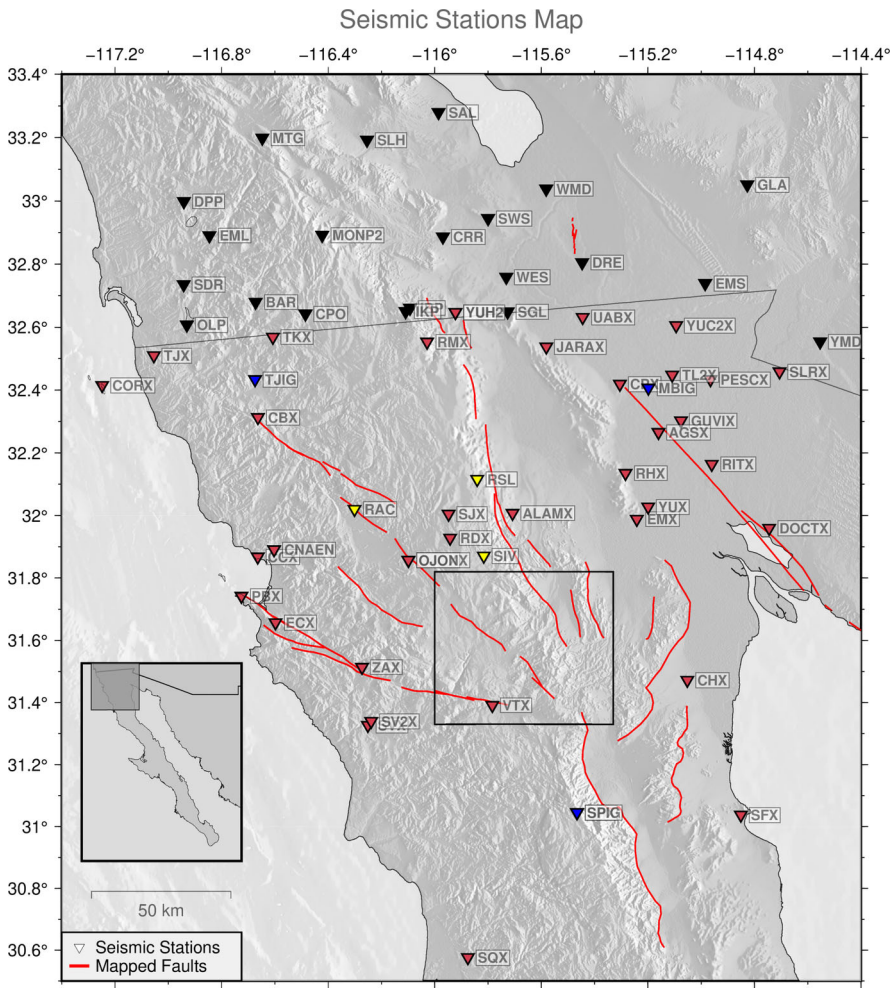

Fig. 2 Study area and station locations of the RESNOM (red), RANM (yellow), SSN (blue), and SCSN (black) seismic networks used to detect and locate the earthquakes analyzed in this study. Station coordinates are listed in Table 1. Not shown are stations PIX (RESNOM), NE80 and PPXB (RESBAN) to the east, PLIB (RESBAN) and HSIG (SSN) to the southeast, and SLGB (RESBAN) to the south

is determined from the S-wave amplitude, corrected for geometrical spreading.

Between January 1, 2010, and December 31, 2024, the RESNOM catalog includes 4010 earthquakes within the study area detected by the stations shown in Fig. 2 and listed in Table 1, with magnitudes ranging from ML 0.3 to 5.1, along with their corresponding waveform data.

Table 1 Seismic stations used for earthquake location

Station Name	Lat	Lon	Station Name	Lat	Lon
AGSX	32.2658	-115.1605	RAC	32.0203	-116.3012
ALAMX	32.0075	-115.7082	RDX	31.9282	-115.9422
BAR	32.68	-116.6722	RHX	32.135	-115.2843
CBX	32.3132	-116.6637	RITX	32.164	-114.9603
CCX	31.8678	-116.6645	RMX	32.5535	-116.0288
CHX	31.472	-115.052	RSL	32.116	-115.8407
CNAEN	31.891	-116.603	SAL	33.28	-115.9858
CORX	32.4153	-117.2482	SDR	32.7357	-116.9423
CPO	32.6427	-116.4852	SFX	31.0375	-114.851
CPX	32.4195	-115.305	SGL	32.6493	-115.7263
CRR	32.8868	-115.9692	SIV	31.8708	-115.816
DOCTX	31.9595	-114.745	SJX	32.0048	-115.948
DPP	32.9987	-116.9415	SLGB	29.83	-114.404
DRE	32.8053	-115.4468	SLH	33.1927	-116.254
ECX	31.657	-116.5978	SLRX	32.4588	-114.706
EML	32.8908	-116.8457	SPIG	31.0458	-115.466
EMS	32.7392	-114.9852	SPX	31.045	-115.466
EMX	31.9882	-115.2417	SQX	30.5762	-115.8758
GLA	33.0515	-114.827	SV2X	31.3398	-116.2385
GUVIX	32.3028	-115.076	SVX	31.327	-116.251
HSIG	29.0197	-110.9492	SWS	32.945	-115.7998
IBP	32.661	-116.0928	TJIG	32.4338	-116.6745
IKP	32.6502	-116.1095	TJX	32.5102	-117.0543
JARAX	32.5378	-115.5815	TKX	32.5687	-116.6075
MBIG	32.407	-115.198	TL2X	32.4482	-115.109
MONP2	32.892	-116.4223	UABX	32.6315	-115.4447
MTG	33.1992	-116.6472	VTX	31.3913	-115.784
NE80	30.5	-112.32	WES	32.759	-115.7315
OJONX	31.8572	-116.099	WMD	33.0382	-115.5818
OJOX	31.8573	-116.0985	YMD	32.554	-114.5535
OLP	32.6078	-116.9303	YUC2X	32.6055	-115.094
PBX	31.742	-116.7255	YUH	32.6473	-115.9225
PESCX	32.4338	-114.965	YUH2	32.6475	-115.9222
PIX	31.5628	-113.4598	YUX	32.0277	-115.199
PLIB	29.9157	-112.6947	ZAX	31.5137	-116.273
PPXB	31.3355	-113.633			

3 Methodology

To obtain more precise hypocentral locations, we relocate the earthquakes using the waveform-based double-difference method (Waldhauser and Ellsworth 2000), which reduces errors caused by unmodeled lateral heterogeneities in the seismic velocity structure that are not represented in the Earth model used for initial hypocentral determination. By focusing on differential measurements between nearby event pairs, the method substantially reduces systematic errors associated with inaccuracies in the assumed Earth model.

The double-difference algorithm is formulated as an iterative least-squares procedure that relates the residuals between observed and predicted differential P- and S-wave arrival times for pairs of earthquakes i and j recorded at the same station k. The residual is expressed as

$$dr_k^{ij} = \left(t_k^i - t_k^j\right)^{\text{obs}} - \left(t_k^i - t_k^j\right)^{\text{cal}}, \tag{1}$$

where $\left(t_k^i - t_k^j\right)^{\text{obs}}$ is the observed travel time difference and $\left(t_k^i - t_k^j\right)^{\text{cal}}$ is the predicted travel time difference based on the initial hypocentral locations. The relationship between these residuals and corrections to the earthquake locations is linearized as

$$\frac{\partial t_k^i}{\partial \mathbf{m}} \Delta \mathbf{m}^i - \frac{\partial t_k^i}{\partial \mathbf{m}} \Delta \mathbf{m}^j = dr_k^{ij}, \tag{2}$$

where $\Delta \mathbf{m}^i = (\Delta x^i, \Delta y^i, \Delta z^i, \Delta \tau^i)$ represents the corrections to the initial source parameters $\mathbf{m} = (x, y, z, \tau)$ for event i, with τ denoting origin time. By solving this system iteratively for many event pairs simultaneously, the method achieves a network of hypocenters with improved relative location accuracy, particularly for tightly clustered seismicity.

To relocate the events from the RESNOM catalog, we computed P- and S-wave travel time differences based on the SJ18 velocity model (Table 2) developed by Ramírez Ramos et al. (2019), which best represents the seismic velocity structure of the Peninsular Ranges of Baja California. The use of an appropriate velocity model further improves the reliability of the relocation, although the double-difference method remains relatively insensitive to large-scale velocity anomalies.

Table 2 SJ18 Model used for relocation of earthquakes

Depth [km]	*P*-Wave Velocity [km/s]
0–4.5	5.6
4.5–9.5	6.8
9.5–18.2	7.3
18.2–	7.9

Recognizing that earthquakes with similar hypocentral locations produce highly similar waveforms — assuming similar rupture processes along the fault— when recorded at the same station, we enhanced the differential time measurements by cross-correlating the waveforms of event pairs. Cross-correlation allows for the determination of relative arrival times with sub-sample precision, reducing random picking errors and further improving the relative locations. For each event pair, we performed waveform cross-correlation on a windowed segment around the P- and S-wave arrivals at each station, accepting measurements only when the correlation coefficient exceeded a specified threshold, which we set to 0.1, thereby ensuring the quality of the differential time dataset.

The resulting relocation dataset provides high-resolution images of the active fault structures in the Valle de la Trinidad region, allowing for the identification of previously unrecognized fault strands and improving the understanding of fault interaction and rupture processes in this complex tectonic setting.

Moment tensor inversion was performed for all earthquakes with M $\geq$ 4 in the study region using the ISOLA software package (Sokos and Zahradnik 2008, 2013), which implements a full-waveform inversion approach in the time domain. This methodology exploits the linear relationship between observed seismograms and Green's functions, wherein the observed ground motion $u(t)$ at a station is modeled as the sum of Green's functions $G_{ij}(t)$ weighted by the corresponding moment tensor elements m_{ij},

$$u(t) = \sum_{i=1}^{3} \sum_{j=i}^{3} G_{ij}(t) m_{ij}. \tag{3}$$

The inversion procedure aims to determine the moment tensor elements that best reproduce the observed seismograms. ISOLA achieves this by minimizing the misfit between observed and synthetic waveforms

through a least-squares approach. Crucially, the method allows for minor phase shifts between observed and synthetic signals to account for unmodeled lateral heterogeneities and velocity anomalies within the Earth structure, enhancing the robustness of the inversion.

Mathematically, the vector **m** containing the moment tensor elements is derived by solving the overdetermined system

$$\mathbf{m} = (G^T G)^{-1} G^T \mathbf{u}, \tag{4}$$

where G is the matrix containing time series of Green's functions for each source-receiver pair and u is the vector of observed waveform data. Synthetic Green's functions were generated assuming a Dirac delta source using the SJ18 velocity model (Ramírez Ramos et al. 2019), consistent with the model used in the relocation stage. A frequency band of 0.02-0.09 Hz was employed in the inversion to maximize the signal-to-noise ratio while preserving sufficient resolution appropriate for moderate-magnitude events.

In tectonic environments, isotropic components in moment tensors of small earthquakes are expected to be negligible (Dziewonski and Woodhouse 1983; Julian et al. 1998). Moreover, in full moment tensor inversions, the isotropic and compensated linear vector dipole (CLVD) components are linearly dependent and share the same polarity; their ratio is governed by the local v_P/v_S velocity ratio and thus remains approximately constant (Vavryčuk 2011, 2001). To reduce spurious non-double-couple (NDC) components, we constrained the isotropic component during the inversion, thereby yielding deviatoric moment tensors.

The quality of each inversion was assessed by calculating the variance reduction (VR), defined as

$$\mathrm{VR} = 1 - \frac{\sum (d_{\mathrm{obs}} - d_{\mathrm{syn}})^2}{\sum (d_{\mathrm{obs}})^2}, \tag{5}$$

where d_{obs} and d_{syn} represent the observed and synthetic waveforms, respectively, summed over all time samples, components, and stations involved. A high variance reduction indicates a close match between observed and synthetic data, implying a reliable inversion result.

Additionally, the size of the CLVD component serves as a complementary indicator of inversion quality. Since most CLVD components in small earthquakes are artifacts without geologic meaning (Rösler and Stein 2022), inversions yielding small CLVD percentages can be considered more reliable. The robustness of the moment tensor solutions is also dependent on the azimuthal coverage and number of seismic stations included in the inversion. A wide and uniform station distribution enhances the resolution of the source mechanism, while inversions based on sparse or azimuthally biased station networks are more prone to instability. Together, these measures serve as indicators of the reliability of the inversion and the likelihood that the derived moment tensors accurately represent the source processes of earthquakes in the Valle de la Trinidad region.

4 Results

Following the 1956 earthquake sequence, the Valle de la Trinidad experienced a quiescence of earthquakes with ML $\geq$ 5 lasting more than 50 years. The largest instrumentally recorded event in the area occurred on April 4, 2010, in the El Mayor-Cucapah mountains, with a magnitude of Mw 7.2. However, the margin of the Baja California microplate remained largely quiet until the ML 5.1 earthquake on February 9, 2015 (Fig. 3a). Despite its magnitude, the aftershock sequence of this event became indistinguishable from background seismicity within weeks, when the number of earthquakes returned to values observed prior to the earthquake. In contrast, a similarly sized earthquake on August 17, 2020, initiated an ongoing seismic sequence that continues to the present day, including six events exceeding Mw 4 and a Mw 4.7 foreshock, and a total of 2862 events to date. The number of earthquakes since the initial event of the sequence is significantly higher than prior to the sequence. Additionally, the b-value (Gutenberg and Richter 1944) decreases markedly at the onset of the sequence, from 1.14 to 0.91 (Fig. 4), indicating a relative increase in larger-magnitude earthquakes. This change suggests a possible transition in the frictional properties along the San Miguel fault — where most of the seismicity is concentrated — from a locked state to one that allows the fault to slip more freely. Consistent with this, the a-value increased at the start of the sequence, reflecting the surge in seismicity following its onset. This alternating pattern of sustained and absent seismic sequences in the Valle de la Trinidad significantly deviates from the conventional mainshock-aftershock sequence. Notably, this

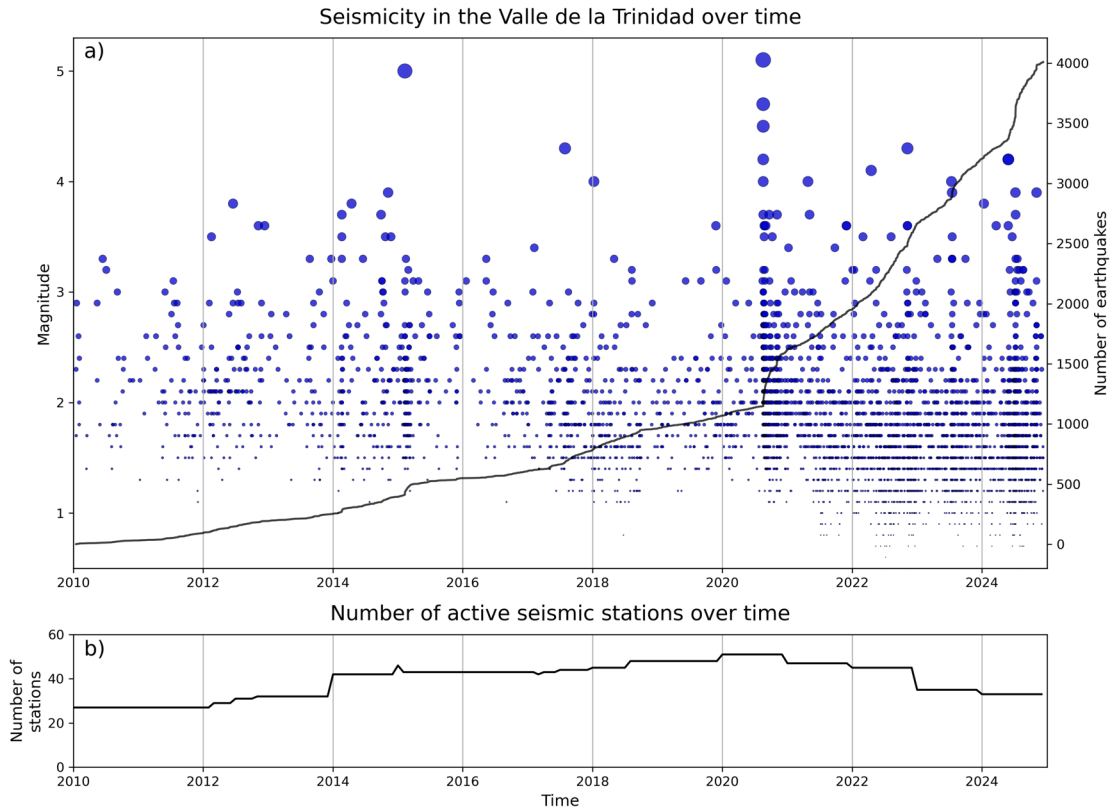

Fig. 3 (a) Temporal distribution of seismicity in the Valle de la Trinidad. (b) Number of active seismic stations over time. The ML 5.1 earthquake on February 9, 2015, was followed by a brief aftershock sequence and did not lead to sustained seismic activity. In contrast, a similarly-sized event on August 17, 2020, initiated a prolonged seismic sequence that continues to the present, with a total of 2862 events recorded in the Valle de la Trinidad. The number of active seismic stations (b) remained relatively stable throughout the study period, with a slight decrease following the onset of the 2020 sequence, suggesting that the observed increase in seismicity is not attributable to changes in network sensitivity

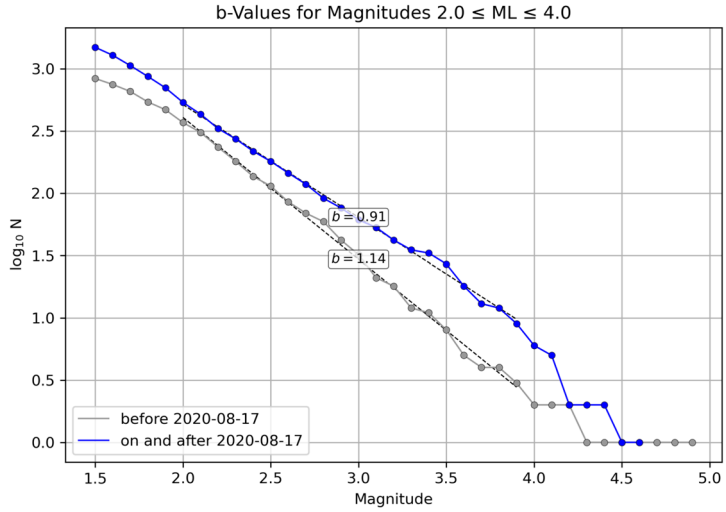

Fig. 4 *b*-values for earthquakes that occurred before, and on or after, August 17, 2020, in the Valle de la Trinidad. A significant decrease is observed at the start of the sequence, indicating a relative increase in larger-magnitude earthquakes, which may suggest a change in the frictional properties along the fault. The minimum and maximum completeness magnitudes are estimated based on deviations from the linear trend

difference is not attributable to changes in network sensitivity; the number of operational seismic stations has slightly decreased since the onset of the current sequence (Fig. 3b).

Relocating the hypocenters of the RESNOM catalog using the double-difference method significantly reduces uncertainties in both epicentral and depth determinations. While the original catalog reports average horizontal and vertical uncertainties of 1618.2 m and 3931.4 m, respectively, for 4,010 events, relocation reduces these to 314.6 m and 337.5 m for the 3,197 events successfully relocated. The relocated epicenters show strong alignment with mapped faults in the region, particularly the San Miguel fault, as delineated by the National Institute of Statistics and Geography (Instituto Nacional de Estadística y Geografía 1982a; Instituto Nacional de Estadística y Geografía 1982b, Fig. 5a). Notably, the relocated events no longer form the diffuse cloud seen in the original RESNOM catalog (Fig. 1), but instead exhibit a clear trend along the fault trace. However, the epicenters also show a clear trend along a structure that intersects the fault. East of the fault, the epicenters cluster into discrete groups without linear alignment (Fig. 5a).

The reduction in uncertainty is particularly significant for hypocentral depths, which are often fixed in standard catalogs when depth resolution is poor - commonly due to limited station coverage or strong lateral heterogeneities in the Earth's crust. The relocated depths show no pronounced clustering in depth in the projection onto the fault (Fig. 5c), consistent with a spatially random distribution of seismicity along a fault zone without abrupt structural discontinuities. Interestingly, the relocated events reveal distinct temporal clustering. A small group of earthquakes in the southeast of the Valle de la Trinidad, possibly due to stress transfer after the February 9, 2015 earthquake, 2054 days after January 1, 2010 (Fig. 5b). In contrast, most of the seismicity along the San Miguel Fault initiated following the three larger earthquakes of August 2020, at day 3881. Immediately after this onset, seismic activity was observed on both sides of the intersection of the fault with the intersecting structure (located at 17 km along the profile in Fig. 5b), with focal depths ranging from 1 to 9 km. By August 2021 (around day 4300), seismicity had migrated to the northwest segment of the fault, forming a narrow band of hypocenters with a width of about 5 km, before shifting abruptly to the southeast in September 2023 (around day 5000). The hypocentral areas during different stages of seismicity do not overlap, consistent with progressive stress release along the fault following each earthquake.

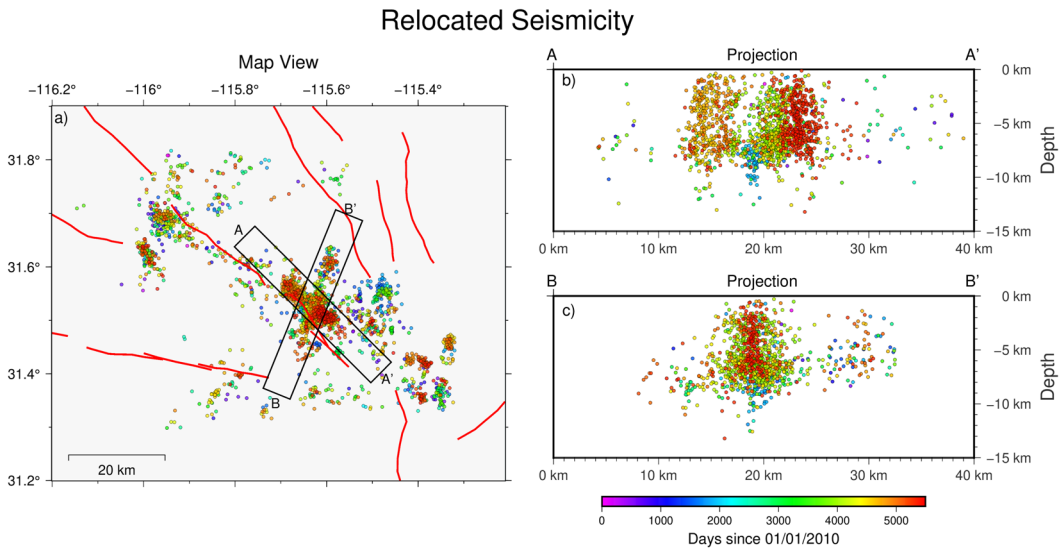

Fig. 5 Map view (a) and cross-sections (b and c) of relocated seismicity from 2010 to 2024. Earthquake locations are clearly aligned with the San Miguel Fault and an intersecting structure. The projection of hypocenters along the San Miguel Fault (A-A') reveals a pattern of seismic migration, with activity initiating and ceasing on either side of the intersection with the unnamed fault. Seismicity along the intersecting fault (B-B') is observed both before and after the onset of the 2020 sequence

Events along the intersecting structure predominantly occurred at greater depths - between 7 and 11 km - prior to the onset of the 2020 sequence at its intersection with the San Miguel fault (Fig. 5c). During the sequence, seismicity forms a narrow band around the intersection, with focal depths similar to those observed along the San Miguel fault. Farther north along the intersecting structure, hypocenters of seismicity unrelated to the 2020 sequence are scattered at comparable depths, suggesting the presence of another seismically active zone along this structure.

The results of the moment tensor inversion are consistent with the dynamics along the San Miguel fault, particularly during the seismic sequence that began in 2020 (Table 3). On August 17, 2020, five events with ML $\geq$ 4 occurred in close proximity in the Valle de la Trinidad (Events 4-9, Fig. 6), initiating a sequence that continues to the present day. The Mw 4.7 foreshock (Event 4), which occurred at 15:09:07 UTC, exhibited a right-lateral strike-slip mechanism. Its fault plane, striking at 298°, aligns closely with the trace of the San Miguel Fault (Table 4). The steep dip of 75° is typical for strike-slip earthquakes and is reflected in a rake of $-177°$. Given the earthquake's magnitude and the preceding seismic quiescence, the certainty of the moment tensor solution is high: the variance reduction reaches 54%, indicating a strong similarity between observed and synthetic waveforms computed for the derived moment tensor. A small CLVD component of -7.2% further confirms the quality of the inversion, which was based on seismograms from nine stations. Nevertheless, the polarity of the small NDC component may hint at the transtensional stress regime characteristic of the Baja California Peninsula, a pattern also reflected in the moment tensors of other regional earthquakes.

The mainshock of the sequence occurred slightly more than 21 minutes after the foreshock (Event 5), at 15:30:33 UTC, and exhibited a nearly identical focal mechanism, with a strike of 305°, a dip of 75°, and a rake of 168°. However, its magnitude was Mw 5.3, releasing approximately eight times more energy than the Mw 4.7 foreshock. Similar to the foreshock, the mainshock achieved a variance reduction of 55% in the moment tensor inversion, based on recordings from nine stations. Its CLVD component is -4.6%, indicating minor dilatational forces along the B-axis.

Two aftershocks with ML $\geq$ 4 occurred in the coda of the mainshock, at 15:31:41 and 15:32:44 (Events 6 and 7, Fig. 7). Due to the superposition of seismic waves from multiple events, moment tensor inversion was successful only for the aftershock at 15:32:44 with

Table 3 Moment tensor solutions for earthquakes with $M_L \geq 4$ between 2010 and 2024

Event No.	Origin Time	Lat	Lon	Depth	M_w	No. Stations	VR	CLVD	Beachball
1	2015-02-09 01:45:03.00	31.527	-115.663	9.0	5.1	7	8%	49.3%	
2	2017-07-29 00:42:25.00	31.357	-115.353	7.0	4.2	9	27%	5.6%	
3	2018-01-07 19:30:21.00	31.615	-115.823	5.5	4.5	6	18%	42.1%	
4	2020-08-17 15:09:07.00	31.501	-115.647	5.9	4.7	9	54%	-7.2%	
5	2020-08-17 15:30:33.00	31.498	-115.643	6.0	5.3	9	55%	-4.6%	
6	2020-08-17 15:31:41.00	31.509	-115.636	5.2	4.2	moment tensor inversion unsuccessful			
7	2020-08-17 15:32:44.00	31.522	-115.623	6.0	4.6	8	20%	-59.8%	
8	2020-08-17 16:29:54.00	31.524	-115.618	6.0	4.0	8	22%	-27.7%	
9	2021-04-26 05:12:05.00	31.501	-115.642	7.0	3.9	12	21%	-19.7%	
10	2022-04-17 05:38:25.00	31.658	-115.950	8.0	3.9	5	52%	17.1%	
11	2022-11-07 04:59:03.00	31.554	-115.688	7.0	4.3	14	55%	-3.8%	
12	2023-07-13 01:42:53.00	31.768	-115.916	12.5	4.8	12	31%	11.9%	
13	2024-05-27 11:05:45.00	31.486	-115.616	5.0	4.4	12	58%	7.9%	
14	2024-05-28 07:47:34.00	31.479	-115.616	5.2	4.3	11	69%	-12.2%	

All data are derived from moment tensor inversion, except for Event 6, for which inversion was unsuccessful due to overlap with the coda of the larger Event 5, which occurred slightly more than a minute earlier. Consequently, the data for Event 6 are taken from the RESNOM catalog. The colors of the stereographic projections indicate different faulting styles

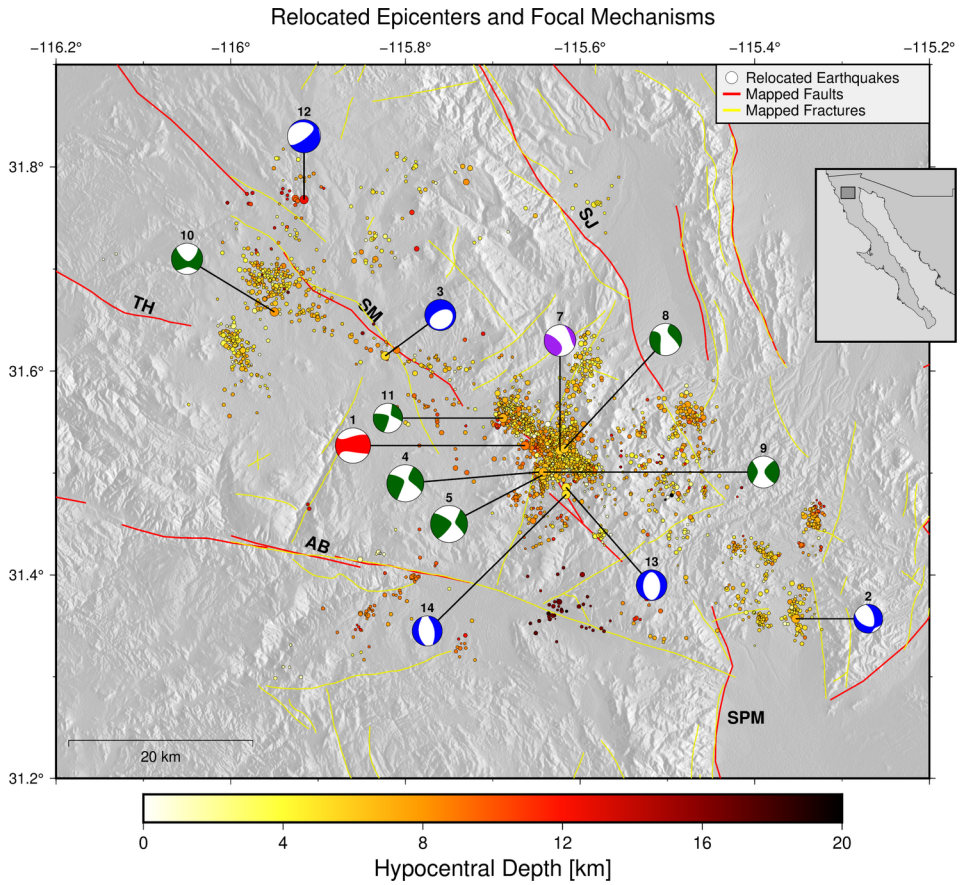

Fig. 6 Map showing the locations and focal mechanisms of the relocated seismic events. Epicenters aligned along a structure that intersects the San Miguel Fault correspond to a feature classified as a fracture by the National Institute of Statistics and Geography (INEGI). Note that the locations derived from moment tensor inversion do not necessarily coincide with those obtained through the relocation process. Focal mechanisms are linked to their respective epicenters as determined by the moment tensor inversion. Stereographic projections are color-coded by faulting style: reverse-faulting earthquakes in red, strike-slip in green, normal-faulting in blue, and oblique-faulting in purple

ML 4.5 (Event 7). However, its variance reduction of 22% was considerably lower than that of the foreshock and mainshock, and only eight stations could be used in the inversion. As a result, the CLVD component is relatively large at -59.8%, despite a fault plane geometry that fits regional geology, with a strike of 118°, a dip of 84°, and a rake of −134°. Interestingly, the polarity of the NDC component is consistent with the extensional component commonly observed along strike-slip faults in the region.

A slightly smaller earthquake occurred at 16:29:54 UTC with a moment magnitude of 4.0 (Event 8). Despite a comparable variance reduction of 22% and the use of 8 stations in the inversion, its CLVD component is notably lower at -27.7% due to a better signal-to-noise ratio. The fault geometry is consistent with other events in the sequence, with a strike of 299°, a dip of 64°, and a rake of −157°.

The following three earthquakes in the sequence with ML $\geq$ 4 (Events 9-11) had focal mechanisms similar to those of the events on August 17, 2020. On April 26, 2021, an Mw 3.9 earthquake (Event 9) occurred in the immediate vicinity of the August 17, 2020 epicenters (Fig. 6), displaying a nearly identical focal mechanism. Its strike of 134°, dip of 83°, and rake of 170° closely match those of the earlier large events and align well with the orientation of the San Miguel fault. The slightly larger CLVD component (-19.7%) may

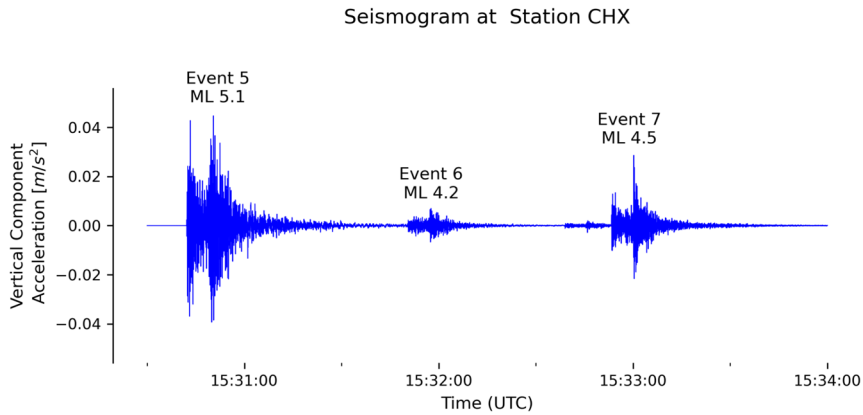

Fig. 7 Vertical-component seismogram recorded at station CHX on August 17, 2020, after removal of the instrument response. Two aftershocks (Events 6 and 7) followed shortly after the mainshock that initiated the ongoing seismic sequence. The proximity in time of the events affected the moment tensor inversion for the aftershocks: no solution could be obtained for event 6, and the solution for event 7 is subject to large uncertainties. In contrast, the moment tensor of event 5 is well constrained

reflect increased noise levels associated with the elevated seismicity during the ongoing sequence, consistent with the lower variance reduction of 21%, despite the use of 12 seismic stations in the inversion. Nevertheless, the polarity of the CLVD component may again indicate a minor normal-faulting contribution, reflecting the transtensional nature of the regional tectonic regime.

Nearly exactly one year later, on April 17, 2022, an earthquake of similar size (Mw 3.9) occurred in the Valle de la Trinidad (Event 10), slightly south of the San Miguel fault, within a cluster of events located northwest of the earlier earthquakes in the sequence (Fig. 6). Nevertheless, its focal mechanism closely resembles those of the previous events in the sequence, with a strike of 138°, a dip of 76°, and a rake of −155°, consistent with the dynamics of the San Miguel fault. Interestingly, the CLVD component of this earthquake is similar in size but opposite in polarity to that of most other events, making it the only one among the seven earthquakes with determined moment tensors in the two years following August 17, 2020 to exhibit a compressional component along the B-axis. The variance reduction for the inversion is high at 52%, but the solution is based on data from only five stations, which may indicate a less well-constrained moment tensor compared to other earthquakes in the sequence - an expected outcome for smaller magnitude events (Rösler et al. 2021).

The epicenter of the Mw 4.3 earthquake that occurred seven months later on November 7, 2022 (Event 11), is located a few kilometers to the northwest of the earthquakes that marked the start of the sequence on August 17, 2020 (Fig. 6), with most seismicity in the sequence occurring in between. It is therefore unsurprising that its focal mechanism closely resembles the those of the events early in the sequence, with a strike of 285°, a dip of 75°, and a rake of 173°. The variance reduction of the moment tensor inversion is high at 55%, and data from 14 stations were used, resulting in a well-constrained solution. The small CLVD component of -3.8% is consistent with the polarity of the NDC components observed in most earthquakes of the sequence.

The seismic sequence continued into 2023 with earthquakes exhibiting different focal mechanisms, notably three normal-faulting events on July 13, 2023, and May 27 and 28, 2024 (Events 12-14). Their dip-slip mechanisms suggest that the CLVD components observed in previous large earthquakes of the sequence may reflect real geological processes, with a normal-faulting component accommodating partial dilatational motion along the San Miguel fault. The variance reduction for the first event is low at 31%, but increases for the later events, reaching 58% and 69%, respectively. All three inversions used a large number of stations (12, 12 and 11, respectively). The resulting CLVD components of 11.9%, 7.9% and -12.2% are therefore interpreted as expected deviations expected deviations from a pure double-couple source due to uncertainties in the Earth model used for the generation of the Green's functions used for the inversion (Rösler et al. 2024) without

geologic significance. Interestingly, these three events occurred to the northwest and the southeast of the main cluster of epicenters of the sequence (Fig. 6), possibly indicating stress transfer from earlier earthquakes in the sequence and the accommodation of extensional stresses at the edges of the tectonically active structure

The focal mechanisms of earthquakes prior to the 2020 sequence (Events 1-3), despite the magnitudes of the events, are much less well constrained and deviate significantly from a pure double-couple source mechanism. The earliest earthquake with ML $\geq$ 4 in our dataset occurred on February 9, 2015 (Event 1), located between the epicenters of the August 17, 2020, and November 7, 2022, events (Fig. 6). Although clearly associated with seismicity along the San Miguel fault, its oblique-slip focal mechanism with components of reverse and strike-slip faulting, exhibits a large CLVD component of 49.3%, indicating a compressional contribution along the B-axis, and thus differing from most other source mechanisms in the sequence. While it cannot be excluded that this NDC component reflects actual geological processes, it is also possible that CLVD components of this magnitude are artifacts of the inversion process (Rösler et al. 2023). The best-fitting double-couple solution for this earthquake yields a strike of 115°, a dip of 61°, and a rake of 133°. Although the fault geometry does not significantly differ from that of the other strike-slip earthquakes in the sequence, the variance reduction is low (8%), and only seven stations were used in the inversion, indicating a high degree of uncertainty in its focal mechanism.

The two other earthquakes that occurred prior to the onset of the sequence, on July 29, 2017 (Event 2), and August 1, 2018 (Event 3), exhibit dip-slip mechanisms. Located to the southeast and northwest of the Valle de la Trinidad (Fig. 6), respectively, their primarily normal-faulting focal mechanisms could reflect variations in the stress regime at the periphery of the area with seismicity during the seismic sequence, suggesting a transition from strike-slip to dip-slip faulting to accommodate the dilatational motion inferred from the CLVD components of the strike-slip earthquakes. However, the variance reductions for these events are low (27% and 18%), and their inversions used only nine and six stations, respectively, indicating less well-constrained moment tensors. Their CLVD components, at 5.6% and 42.1%, further reflect these uncertainties. Additionally, the fault geometries of these two events differ significantly from the dominant fault orientations in the region, further reducing confidence in the robustness of their focal mechanism solutions.

5 Discussion

Relocating hypocenters of earthquakes detected with the RESNOM seismic network using waveform-based double-difference method reveals that the hypocenters are well-aligned with mapped faults in the Valle de la Trinidad, which lies at the convergence of the Agua Blanca (AB), Tres Hermanos (TH), San Miguel (SM), San Pedro Mártir (SPM) and Sierra Juárez (SJ) faults. From 2010 to 2024, seismicity is primarily associated with the San Miguel fault, but also with a cross-cutting structure that intersects it, previously classified as a fracture by the National Institute of Statistics and Geography (INEGI, Fig. 6) and thus thought to be seismically inactive. Although seismically much less active than the San Miguel fault, relocation of hypocenters reveals that seismicity is associated with this structure, making it necessary to classify it as a fault with potential to host a larger earthquake.

Seismicity on this structure occurs both before the ML 5.1 earthquake of February 9, 2015 and the start of the seismic sequence on August 17, 2020, with epicenters separated from the intersection to the San Miguel fault. Therefore, seismicity on the structure is not triggered by any of the larger earthquakes but rather occurs due to the accommodation of stresses along the structure. However, it seems likely that seismicity is caused by stress transfer from the numerous nearby faults.

Relocation places the epicenter of the Mw 5.1 mainshock of the seismic sequence on August 17, 2020, approximately 4 km south of the intersection between the previously unmapped fault and the San Miguel fault, in close proximity to its Mw 4.7 foreshock earlier the same day. Both earthquakes exhibit strike-slip focal mechanisms, with one nodal plane aligned with the San Miguel fault and the other with the intersecting structure, making it possible - though unlikely - that rupture occurred along the intersecting structure during these events. The nearly identical epicenter of the February 14, 1956, ML 6.3 earthquake could support this hypothesis; however, the location of the 1956 event is highly uncertain due to the absence of digital seismograms. Therefore, we consider it most likely that rupture during these three earthquakes involved both the San Miguel Fault and the intersecting structure,

consistent with the observation that the largest events occurred precisely at their intersection. Nevertheless, moment tensor inversion cannot distinguish which fault plane accommodated slip in the case of conjugate faults, as their radiation patterns are identical. Simultaneous rupture on both faults would also be consistent with the low CLVD components observed in the moment tensor solutions, as the conjugate geometry of the fault planes would mask a complex rupture as a simple focal mechanism.

Simultaneous rupture on conjugate faults has been reported in several tectonic settings along the western margin of the North American plate. In the San Jacinto Fault Zone, Ross et al. (2017) documented interlaced strike-slip and normal faults, along with fault structures nearly orthogonal to the trend of the San Jacinto fault. Similarly, during the 2019 Ridgecrest earthquake sequence, seismicity illuminated two nearly orthogonal fault systems: Shelly (2020) and Li et al. (2020) both identified crosscutting northwest- and southwest-striking alignments, confirming the complex conjugate faulting pattern. On the Baja California peninsula, Doser (1992) suggested that the rupture processes of the 1956 M≥6 events associated with the San Miguel Fault were influenced by cross faults intersecting its main trace. More recently, Vidal et al. (2010) analyzed rupture processes of earthquakes with magnitudes $4.1 \leq \mathrm{ML} \leq 5.3$ in the Peninsular Ranges of Baja California and found that the ML 5.3 earthquake of December 3, 1991, had a focal mechanism with a nodal plane nearly perpendicular to the San Miguel and Sierra Juárez faults. However, they noted that no surface trace could be associated with this intersecting plane, preventing an unambiguous identification of the fault that ruptured during the event. In the Valle de la Trinidad seismic sequence, the mainshock was followed by a series of aftershocks along the intersecting structure, suggesting that rupture either occurred on or extended onto the intersecting structure during the mainshock.

Foreshocks of smaller magnitude may dynamically or statically trigger the rupture of a subsequent larger mainshock in complex fault systems, particularly when the events occur on intersecting or orthogonal fault systems. This phenomenon was observed during the 2019 Ridgecrest earthquake sequence, where a Mw 6.4 foreshock preceded the Mw 7.1 mainshock by approximately 34 hours (Hauksson and Jones 2020). Seismic and geodetic analyses revealed that the Mw 6.4 event ruptured a southwest-striking fault, while the subsequent Mw 7.1 event occurred on a nearly orthogonal northwest-striking fault, highlighting the complexity of stress transfer and fault interaction in fault networks with conjugate geometries.

To investigate whether a similar interaction between intersecting faults occurred during the August 17, 2020 mainshock (event 5), we correlated its waveforms with those of all other events with successful moment tensor inversions, as well as event 6 (Table 3). Using TauP (Crotwell et al. 1999) to calculate P-wave arrival times, we normalized the seismograms, allowed for time shifts, and computed the highest correlations across all stations and components, testing multiple frequency bands. In the frequency band used for the inversion (0.02–0.09 Hz), event 5 most closely matches its foreshock (event 4, Fig. 8), event 1, and events 8 and 9. Other frequency bands yield consistent patterns of similarity, albeit with lower correlation coefficients, as expected for higher frequencies. While similarity with the foreshock is expected, the focal mechanism of event 1 differs markedly from those of events 8 and 9: event 1 contains a compressional NDC component, whereas events 8 and 9 exhibit extensional NDC components consistent with the regional transtensional regime — a contrast that further supports the interpretation that the NDC component of event 1 is an artifact of the moment tensor inversion (Rösler and Stein 2022). Both events 8 and 9 occurred near the intersection of the San Miguel Fault with the cross-cutting structure, suggesting that both faults may have been involved in the rupture of event 5, though definitive proof remains absent without a large event on the intersecting structure for comparison.

The waveform correlations and focal mechanism patterns for the August 2020 sequence point to possible rupture across intersecting faults. Within this sequence, the ML 4.7 earthquake preceded the ML 5.1 mainshock by approximately 21 minutes. Both events occurred near the intersection of the San Miguel fault and the intersecting structure. Although available data do not allow for a definitive determination of whether the ML 4.7 foreshock actively triggered the ML 5.1 mainshock, the spatial and temporal proximity of the events suggests a potential causal relationship. The orientation of the foreshock's nodal planes, one of which aligns with the intersecting structure, further supports the plausibility of stress transfer between adjacent faults.

Recognizing the possibility of foreshock-triggered mainshocks is critical for understanding seismic hazard,

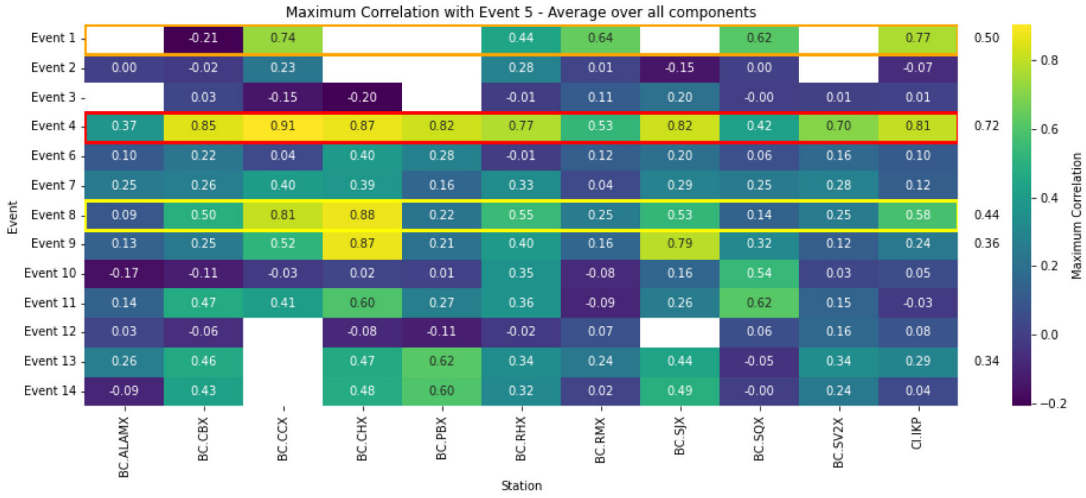

(a) The waveforms of event 5 are most similar to those of its foreshock (event 4) and to events 1 and 8, both of which ruptured the San Miguel fault. However, the location of event 5, south of this fault, suggests that both faults may have been involved in its rupture.

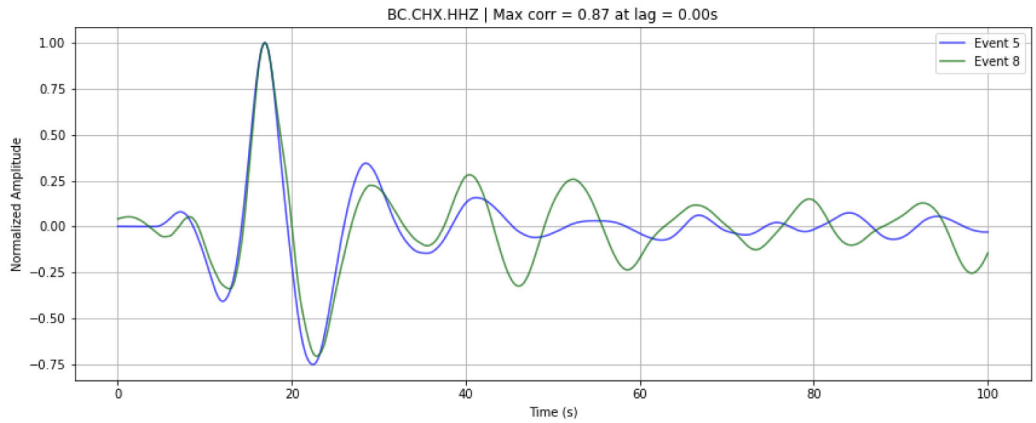

(b) Example for the similarity of the waveforms of events 5 and 8 at station CHX, to the east of the Valle de la Trinidad.

Fig. 8 Results of the waveform similarity analysis to determine which fault ruptured during the August 17, 2020 mainshock (event 5)

particularly in regions like the Peninsular Ranges of Baja California where complex fault interactions appear to be common. Triggering can modify the stress field in a localized area, promoting rupture on neighboring faults that may not have been critically stressed prior to the foreshock. This dynamic interaction challenges traditional models that consider mainshocks as isolated phenomena.

Although the observed sequence of moment tensors could be purely coincidental, it is noteworthy that dip-slip earthquakes in our dataset occur both before the onset of the seismic sequence in the Valle de la Trinidad on August 17, 2020, and again in its later stages in 2024. In contrast, the foreshock, mainshock, and subsequent aftershocks through 2022 all exhibit right-lateral strike-slip mechanisms, consistent with the dynamics along the San Miguel Fault. Normal-faulting earthquakes with ML ≥ 4 were recorded in 2017, 2018, and again in 2024, suggesting that the extensional motion - inferred from the NDC components of many strike-slip earthquakes - may be accommodated at different times than lateral motion, possibly indicating an alternating

pattern between strike-slip and dip-slip faulting styles. However, confirming this hypothesis would require a longer seismic record, which is currently not available for the study area.

6 Conclusions

In this study, we investigated the seismicity and active structures of the Valle de la Trinidad region in northern Baja California between 2010 and 2024. Using waveform-based double-difference relocation of earthquakes recorded by the RESNOM seismic network, we significantly reduced the uncertainties in both epicentral and depth determinations. The relocated hypocenters reveal strong alignment with the San Miguel fault as well as an intersecting structure, previously classified as a fracture. Our results demonstrate that this intersecting structure is seismically active and should be reclassified as a fault capable of hosting moderate to large earthquakes.

The August 17, 2020 seismic sequence, initiated by an ML 4.7 foreshock followed by an ML 5.1 mainshock, illuminated the complex interaction between the San Miguel fault and the intersecting structure. Moment tensor analysis shows that both events exhibit right-lateral strike-slip mechanisms, with nodal planes aligned with both structures. Although moment tensor inversion cannot unambiguously resolve the fault plane due to the conjugate orientation of the faults, the spatial distribution of aftershocks suggests that rupture either occurred on or extended onto the intersecting structure. The low CLVD components observed in the moment tensors support a simple rupture geometry consistent including slip on conjugate faults.

Throughout the 2020-2024 sequence, seismicity migrated spatially along both the San Miguel fault and the intersecting structure, with later stages showing a transition to dip-slip focal mechanisms. This alternating pattern between strike-slip and normal faulting may reflect temporal variations in the local stress field, although longer-term seismic records are needed to confirm this behavior.

The findings of this study underscore the importance of fault intersections in controlling seismic hazard in the Peninsular Ranges of Baja California. Recognizing the activity of the intersecting structure and its potential involvement in large earthquakes improves our understanding of the regional stress regime and highlights the need for updated fault mapping in northern Baja California. Future work integrating geodetic data and dynamic rupture modeling will be essential to fully resolve the role of fault interactions in this seismically complex region.

Appendix

Table 4 Moment tensor components and fault parameters for earthquakes with $M_L \geq 4$ between 2010 and 2024

Origin Time	M_0	M_{rr}	$M_{\theta\theta}$	$M_{\phi\phi}$	$M_{r\theta}$	$M_{r\phi}$	$M_{\theta\phi}$	Strike	Dip	Rake
2015-02-09 01:45:03.00	$4.809e+16$	2.973	-5.179	2.206	0.971	-1.218	-0.663	115°	61°	133°
2017-07-29 00:42:25.00	$2.134e+15$	-1.548	0.481	1.067	-0.580	-0.854	-1.267	349°	57°	−53°
2018-01-07 19:30:21.00	$6.160e+15$	-4.235	1.949	2.286	4.482	1.849	0.983	38°	20°	−112°
2020-08-17 15:09:07.00	$1.134e+16$	-0.695	-8.574	9.269	1.701	2.365	-6.342	298°	75°	−177°
2020-08-17 15:30:33.00	$1.158e+17$	0.101	-1.095	0.994	-0.014	0.374	-0.321	305°	75°	168°
2020-08-17 15:31:41.00	–	moment tensor inversion unsuccessful								
2020-08-17 15:32:44.00	$8.028e+15$	-1.730	-2.724	4.454	-3.949	3.696	-4.479	118°	84°	−134°
2020-08-17 16:29:54.00	$1.083e+15$	-4.091	-4.958	9.049	3.272	2.207	-6.331	299°	64°	−157°
2021-04-26 05:12:05.00	$8.816e+14$	-0.488	-8.319	8.807	0.219	-2.041	-0.087	134°	83°	170°
2022-04-17 05:38:25.00	$7.022e+14$	-0.983	-5.614	6.597	-3.268	0.794	0.021	138°	76°	−155°
2022-11-07 04:59:03.00	$2.842e+15$	0.133	-1.520	1.387	-0.119	0.810	-2.298	285°	75°	173°
2023-07-13 01:42:53.00	$1.808e+16$	-0.715	0.851	-0.136	-1.221	-1.066	0.119	287°	18°	−38°
2024-05-27 11:05:45.00	$5.175e+15$	-5.218	0.151	5.067	0.559	-0.043	-0.068	353°	46°	−98°
2024-05-28 07:47:34.00	$3.745e+15$	-3.571	-0.172	3.743	0.278	-0.502	-0.552	349°	49°	−95°

Data and resources

Both waveform data and the earthquake catalog used in this study was downloaded from the Seismic Network of Northwest Mexico (RESNOM), operated by the Center for Scientific Research and Higher Education at Ensenada (CICESE). Waveform-based double-difference relocation was carried out using HypoDD (Waldhauser and Ellsworth 2000), and moment tensors were obtained through ISOLA (Sokos and Zahradnik 2008, 2013), both using the SJ18 model by Ramírez Ramos et al. (2019) for the Peninsular Ranges of Baja California.

Acknowledgements We gratefully acknowledge the financial and logistical support provided by the CICESE throughout the project. This work was partially funded by internal projects No. PI-641196, PI-64198, PI-641195, PI-641199, and CONACYT project CF-194151. The authors thank an anonymous reviewer and Simone Cesca for their constructive reviews and valuable suggestions, which significantly contributed to the improvement of the manuscript.

Author contributions Boris Rösler drafted the manuscript, conducted the analysis of results, and coordinated the project. Oscar Castro-Artola carried out the earthquake relocation, prepared the figures, and assisted in the interpretation of results. Alejandra Martínez was participated in developing the concept of the study and assisted in writing the manuscript. Carlos E. Reinoza contributed to developing the concept of the study and assisted in the coordination of the project. Luis Yegres carried out the moment tensor inversion. J. Antonio Vidal-Villegas made valuable suggestions that refined both the study concept and the manuscript. Similarly, Franck A. Audemard M. provided insightful comments that led to improvements in the conceptual framework and the manuscript. All authors reviewed the manuscript.

Declarations

Competing interests The authors declare no competing interests.

References

Angelier J, Colletta B, Chorowicz J, Ortlieb L, Rangin C (1981) Fault tectonics of the Baja California Peninsula and the opening of the Sea of Cortez, Mexico. J Struct Geol 4(3):1412–1431. https://doi.org/10.1016/0191-8141(81)90035-3

Atwater T (1970) Implications of plate tectonics for the Cenozoic tectonic evolution of western North America. Bull Seismol Soc Am 12(81):3513–3536. https://doi.org/10.1130/0016-7606(1970)81[3513:IOPTFT]2.0.CO;2

Bennett RA, Rodi W, Reilinger RE (1996) Global Positioning System constraints on fault slip rates in southern California and northern Baja, Mexico. J Geophys Res Solid Earth B10(101):21943–21960. https://doi.org/10.1029/96JB02488

Castro RR, Mendoza-Camberos A, Pérez-Vertti A (2018) The broadband seismological network (RESBAN) of the Gulf of California, Mexico. Seismol Res Lett 2A(89):338–344. https://doi.org/10.1785/0220170117

Crotwell HP, Owens TJ, Ritsema J (1999) The TauP toolkit: flexible seismic travel-time and Ray-path utilities. Seismol Res Lett 70(2):154–160. https://doi.org/10.1785/gssrl.70.2.154

Dixon TH, Miller M, Farina F, Wang H, Johnson D (2000) Present-day motion of the Sierra Nevada block and some tectonic implications for the Basin and Range province, North American Cordillera. Tectonics 1(19):1–24. https://doi.org/10.1029/1998TC001088

Dokka RK, Travis CJ (1990) Late Cenozoic strike-slip faulting in the Mojave Desert, California. Tectonics 2(9):311–340. https://doi.org/10.1029/TC009i002p00311

Dokka RK, Travis CJ (1990) Role of the eastern California shear zone in accommodating Pacific-North American plate motion. Tectonics 9(17):1323–1326. https://doi.org/10.1029/GL017i009p01323

Doser DI (1992) Faulting processes of the 1956 San Miguel, Baja California, earthquake sequence. Pure Appl Geophys 1(139):3–16. https://doi.org/10.1007/BF00876824

Dziewonski AM, Woodhouse JH (1983) An experiment in systematic study of global seismicity: centroid-moment tensor solutions for 201 moderate and large earthquakes of 1981. J Geophys Res Solid Earth B4(88):3247–3271. https://doi.org/10.1029/JB088iB04p03247

Gutenberg B, Richter CF (1944) Frequency of earthquakes in California. Bull Seismol Soc Am 34(4):185–188

Hauksson E, Jones LM (2020) Seismicity, stress state, and style of faulting of the Ridgecrest-Coso region from the 1930s to 2019: seismotectonics of an evolving plate boundary segment. Bull Seismol Soc Am 4(110):1457–1473. https://doi.org/10.1785/0120200051

Hirabayashi CK, Rockwell TK, Wesnousky SG, Stirling MW, Suarez-Vidal F (1996) A neotectonic study of the San Miguel-Vallecitos fault, Baja California, Mexico. Bull Seismol Soc Am 6(86):1770–1783. https://doi.org/10.1785/BSSA0860061770

Hutton K, Hauksson E, Clinton J, Franck J, Guarino A, Scheckel N, Given D, Yong A (2006) Southern California seismic network update. Seismol Res Lett 3(77):389–395. https://doi.org/10.1785/gssrl.77.3.389

Instituto Nacional de Estadística y Geografía (1982a) Conjunto de datos vectoriales geológicos, Ensenada, H11-2, escala 1:250,000, serie I. https://www.inegi.org.mx/app/biblioteca/ficha.html?upc=702825675387 Accessed on 28 Apr 2025

Instituto Nacional de Estadística y Geografía (1982b) Conjunto de datos vectoriales geológicos, San Felipe, H11-3, escala 1:250,000, serie I. https://www.inegi.org.mx/app/biblioteca/ficha.html?upc=702825675394 Accessed on 28 Apr 2025

Johnson TL, Madrid J, Koczynski T (1976) A study of microseismicity in northern Baja California, Mexico. Bull Seismol Soc Am 6(66):1921–1929. https://doi.org/10.1785/BSSA0660061921

Julian BR, Miller AD, Foulger GR (1998) Non-double-couple earthquakes 1. Theory. Rev Geophys 36(4):525–549. https://doi.org/10.1029/98RG00716

Li S, Chen G, Tao T, He P, Ding K, Zou R, Li J, Wang Q (2020) The 2019 Mw 6.4 and Mw 7.1 Ridgecrest earthquake sequence in eastern California: rupture on a conjugate fault

structure revealed by GPS and InSAR measurements. Geophys J Int 3(221):1651–1666. https://doi.org/10.1093/gji/ggaa099

Miller MM, Johnson DJ, Dixon TH, Dokka RK (2001) Refined kinematics of the Eastern California shear zone from GPS observations, 1993–1998. J Geophys Res Solid Earth B2(106):2245–2263. https://doi.org/10.1029/2000JB900328

Pérez-Campos X, Espíndola VH, Pérez J, Estrada JA, Cárdenas Monroy C, Bello D, González-López A, González Ávila D, Esparza Contreras Ruiz, M. G., Maldonado, R., Tan, Y., Rodríguez Rasilla, I., Vela Rosas, M. Á., Cruz, J. L., Cárdenas, A., Navarro Estrada, F., Hurtado, A., Mendoza Carvajal, A. J., Montoya-Quintanar, E., & Pérez-Velázquez, M. A. (2018) The Mexican National Seismological Service: an overview. Seismol Res Lett 2A(89):318–323. https://doi.org/10.1785/0220170186

Petroy DE, Wiens DA (1989) Historical seismicity and implications for a diffuse plate convergence in the Northeast Indian Ocean. J Geophys Res 94(B9):12301–12319. https://doi.org/10.1029/JB094iB09p12301

Plattner C, Malservisi R, Dixon TH, LaFemina P, Sella GF, Fletcher J, Suarez-Vidal F (2007) New constraints on relative motion between the Pacific Plate and Baja California microplate (Mexico) from GPS measurements. Geophys J Int 3(170):1373–1380. https://doi.org/10.1111/j.1365-246X.2007.03494.x

Ramírez Ramos EE, Vidal-Villegas JA, Ramírez-Hernández J, González-Fernández A, Stock JM (2019) A crustal velocity model for the peninsular ranges of Baja California and Southwestern Laguna Salada, Mexico. Seismol Res Lett 3(90):1219–1229. https://doi.org/10.1785/0220180248

Reyes A, Brune J, Barker T, Canales L, Madrid J, Rebollar J, Munguia L (1975) A microearthquake survey of the San Miguel fault zone, Baja California, Mexico. Geophys Res Lett 2(2):56–59. https://doi.org/10.1029/GL002i002p00056

Rösler B, Stein S (2022) Consistency of non-double-couple components of seismic moment tensors with earthquake magnitude and mechanism. Seismol Res Lett 93(3):1510–1523. https://doi.org/10.1785/0220210188

Rösler B, Stein S, Spencer BD (2021) Uncertainties in seismic moment tensors inferred from differences between global catalogs. Seismol Res Lett 92(6):3698–3711. https://doi.org/10.1785/0220210066

Rösler B, Stein S, Ringler AT, Vackář J (2024) Apparent non-double-couple components as artifacts of moment tensor inversion. Seismica 3(1). https://doi.org/10.26443/seismica.v3i1.1157

Rösler B, Stein S, Spencer BD (2023) When are non-double-couple components of seismic moment tensors reliable? Seismica 2(1). https://doi.org/10.26443/seismica.v2i1.241

Ross ZE, Hauksson E, Ben-Zion Y (2017) Abundant off-fault seismicity and orthogonal structures in the San Jacinto fault zone. Sci Adv 3(3). https://doi.org/10.1126/sciadv.1601946

Sauber J, Thatcher W, Solomon SC (1986) Geodetic measurement of deformation in the central Mojave Desert, California. J Geophys Res Solid Earth B12(91):12683–12693. https://doi.org/10.1029/JB091iB12p12683

Sauber J, Thatcher W, Solomon SC, Lisowski M (1994) Geodetic slip rate for the eastern California shear zone and the recurrence time of Mojave Desert earthquakes. Nature 6460(367):264–266. https://doi.org/10.1038/367264a0

Savage JC, Lisowski M, Prescott WH (1990) An apparent shear zone trending north-northwest across the Mojave Desert into Owens Valley, eastern California. Geophys Res Lett 12(17):2113–2116. https://doi.org/10.1029/GL017i012p02113

Shelly DR (2020) A high-resolution seismic catalog for the initial 2019 Ridgecrest earthquake sequence: Foreshocks, aftershocks, and faulting complexity. Seismol Res Lett 4(91):1971–1978. https://doi.org/10.1785/0220190309

Shor GG Jr, Roberts E (1958) San Miguel, Baja California Norte, earthquakes of February, 1956: a field report. Bull Seismol Soc Am 2(48):101–116. https://doi.org/10.1785/BSSA0480020101

Sokos EN, Zahradnik J (2008) ISOLA a Fortran code and a Matlab GUI to perform multiple-point source inversion of seismic data. Comput Geosci 8(34):967–977. https://doi.org/10.1016/j.cageo.2007.07.005

Sokos EN, Zahradnik J (2013) Evaluating centroid-moment-tensor uncertainty in the new version of ISOLA software. Seismol Res Lett 4(84):656–665. https://doi.org/10.1785/0220130002

Thatcher W, Savage JC, Simpson RW (2016) The eastern California shear zone as the northward extension of the southern San Andreas fault. J Geophys Res Solid Earth 4(121):2904–2914. https://doi.org/10.1002/2015JB012678

Vavryčuk V (2011) Tensile earthquakes: theory, modeling, and inversion. J Geophys Res Solid Earth B12(116). https://doi.org/10.1029/2011JB008770

Vavryčuk V (2001) Inversion for parameters of tensile earthquakes. J Geophys Res Solid Earth B8(106):16339–16355. https://doi.org/10.1029/2001JB000372

Vidal A, Munguía L, Gonzaález-García JJ (2010) Faulting parameters of earthquakes ($4.1 \leq ML \leq 5.3$) in the Peninsular ranges of Baja California, Mexico. Seismol Res Lett 1(81):44–52. https://doi.org/10.1785/gssrl.81.1.44

Vidal-Villegas JA, Munguía L, González-Ortega JA, Nuñez Leal MA, Ramírez E, Mendoza L, Castro RR, Wong V (2018) The Northwest Mexico Seismic Network: Real-time seismic monitoring in northern Baja California and northwestern Sonora, Mexico. Seismol Res Lett 2A(89):324–337. https://doi.org/10.1785/0220170183

Waldhauser F, Ellsworth WL (2000) A double-difference earthquake location algorithm: method and application to the northern Hayward fault, California. Bull Seismol Soc Am 6(90):1353–1368. https://doi.org/10.1785/0120000006